SPECIAL
Air-sea interaction during PISTON-MISOBOB-CAMP2Ex
COLLECTION

Stratified Shear Instabilities in Diurnal Warm Layers

KENNETH G. HUGHES,[a] JAMES N. MOUM,[a] EMILY L. SHROYER,[a] AND WILLIAM D. SMYTH[a]

[a] *College of Earth, Ocean, and Atmospheric Sciences, Oregon State University, Corvallis, Oregon*

(Manuscript received 7 December 2020, in final form 18 March 2021)

ABSTRACT: In low winds ($\lesssim 2\,\mathrm{m\,s^{-1}}$), diurnal warm layers form, but shear in the near-surface jet is too weak to generate shear instability and mixing. In high winds ($\gtrsim 8\,\mathrm{m\,s^{-1}}$), surface heat is rapidly mixed downward and diurnal warm layers do not form. Under moderate winds of 3–5 $\mathrm{m\,s^{-1}}$, the jet persists for several hours in a state that is susceptible to shear instability. We observe low Richardson numbers of $\mathrm{Ri} \approx 0.1$ in the top 2 m between 1000 and 1600 local time (LT) (from 4 h after sunrise to 2 h before sunset). Despite Ri being well below the $\mathrm{Ri} = 1/4$ threshold, instabilities do not grow quickly, nor do they overturn. The stabilizing influence of the sea surface limits growth, a result demonstrated by both linear stability analysis and two-dimensional simulations initialized from observed profiles. In some cases, growth rates are sufficiently small ($\ll 1\,\mathrm{h^{-1}}$) that mixing is not expected even though $\mathrm{Ri} < 1/4$. This changes around 1600–1700 LT. Thereafter, convective cooling causes the region of unstable flow to move downward, away from the surface. This allows shear instabilities to grow an order-of-magnitude faster and mix effectively. We corroborate the overall observed diurnal cycle of instability with a freely evolving, two-dimensional simulation that is initialized from rest before sunrise.

KEYWORDS: Tropics; Instability; Turbulence; Diurnal effects

1. Introduction

Sunlight absorbed in the near-surface ocean in low winds causes vertical temperature gradients of $T_z = O(0.1\text{–}1)^\circ\,\mathrm{C\,m^{-1}}$ over the top few meters. The wind's momentum is captured in this thin, stable layer termed a diurnal warm layer (DWL). This forms a diurnal jet that moves at 0.1–0.2 $\mathrm{m\,s^{-1}}$. Except in low winds ($<2\,\mathrm{m\,s^{-1}}$), the gradient Richardson number is often below 1/4 (Kudryavtsev and Soloviev 1990; Sutherland et al. 2016; Hughes et al. 2020a), and therefore the jet satisfies the criterion for stratified shear instability. Enhanced turbulence has been observed as a result, but lacking is a characterization of the instabilities: how quickly they grow, whether they overturn, how they evolve throughout the day, and their horizontal and vertical length scales. In general, such properties govern when and how turbulence mixes away shear and stratification (e.g., Carpenter et al. 2013; Caulfield 2021).

Lake studies provide most of what is known about near-surface instabilities on a geophysical scale. A lack of swell and the potential for sampling upward from a shallow lake floor results in datasets that are more complete than typically possible in the open ocean. Some studies have identified narrowband oscillations following a wind spike (e.g., Thorpe and Hall 1977; Antenucci and Imberger 2001; Gímez-Giraldo et al. 2008; Tedford et al. 2014). Observed characteristics of the oscillations agree with instabilities predicted from the mean shear and stratification.

From a stability analysis using the mean of 25 profiles of velocity and density over 7 h of a daytime period in Loch Ness, Thorpe and Liu (2009) suggested that the instability be characterized as asymmetric Holmboe instability. Earlier work had suggested that Kelvin–Helmholtz instability causes the observed "temperature ramps" with wavelengths of $O(100)$ m (Thorpe and Hall 1977; Thorpe 1978). The revised characterization was not intended as definitive, and inferences of Kelvin–Helmholtz instability in DWLs remain common (Soloviev and Lukas 1996; Moulin et al. 2018; Wijesekera et al. 2020).

The asymmetry that Thorpe and Liu (2009) were referring to is the vertical offset between interfaces of velocity and density (or equivalently shear and stratification) of the background mean flow. Without an offset, Holmboe instability manifests as wisps of fluid ejected from cusps in isopycnal perturbations (Holmboe 1962; Smyth et al. 2007). The resulting turbulence scours the interface (Salehipour et al. 2016), rather than mixing it away through large-scale overturning of the central isopycnal as occurs with the conspicuous billow structure of Kelvin–Helmholtz instability. An offset blurs the boundary between pure Holmboe and Kelvin–Helmholtz instabilities (Carpenter et al. 2010).

The sea surface further complicates the instability characterization. Boundaries tend to suppress the rate at which instabilities grow (Hazel 1972; Yonemitsu et al. 1996; Haigh and Lawrence 1999). This control will vary as the shear and stratification evolve over a diurnal cycle.

Here we use a surface-following platform (section 2) to identify conditions in which instabilities occur (section 3). Thereafter, we focus on one particular day when the near-

Corresponding author: Kenneth G. Hughes, kenneth.hughes@oregonstate.edu

DOI: 10.1175/JPO-D-20-0300.1

surface flow is persistently unstable. From late morning to midafternoon, instabilities grow slowly, being stabilized by the proximity to the sea surface (section 4). Instabilities are able to grow quickly later in the day once convective cooling starts to homogenize temperature and velocity in the top 2 m (section 5). More generally, instability growth is sensitive to the details of near-surface vorticity and how it is affected by wind-, wave-, and buoyancy-driven turbulence (section 6).

2. Equipment and measurements

We present data obtained from a surface-following platform, SurfOtter, from a 2019 field campaign in the tropical western Pacific Ocean (18°N, 126°E) as part of the PISTON project (e.g., Sobel et al. 2021). Briefly, SurfOtter is a 2-m-long aluminum tube with a fin and weighted cable towed beside a ship. It hosts sensors to measure the temperature across the top 5 m and the velocity across the top 10 m continuously for days to weeks. It is more fully described in two prior papers (Hughes et al. 2020a,b). Those papers discuss datasets from 2018 that are similar, but less complete, than the newer dataset to be described here. In 2019, we achieved velocity measurements much closer to the surface. Together with simultaneous measurements of temperature and turbulence, we can now characterize shear instabilities leading to turbulence as well as observationally investigate a hypothesis, developed from simulations, that DWLs in low winds are not subject to instability (Hughes et al. 2020a).

SurfOtter was equipped with an acoustic Doppler current profiler (ADCP) pitched forward by 30° to avoid acoustic interference from SurfOtter itself. With this arrangement, we measured velocities at 0.7–10 m deep with 0.25-m vertical resolution. We measured temperature concurrently with 20 instruments spanning 0.1–5.3 m deep and sampling at 0.16–16 Hz, with most being RBR Solo T loggers at 2 Hz. Temperature measurements were intercalibrated, aligned in time, and smoothed to and resampled at 0.5 Hz. For the purposes of contour plots and calculations of isotherm depth anomalies, we apply a 15-s low-pass filter to minimize the small surface-wave-induced temperature signal (Hughes et al. 2020b). Concurrent vertical profiling from the stern of the ship provided an estimate of temperature at 10 m every 7–10 min.

Here we use 10- and 60-min averages of shear and stratification to interpret instabilities. The shorter time scale is sufficient to filter out surface gravity waves, whereas the longer scale is used for the linear stability analysis following Sun et al. (1998) and Smyth et al. (2011). We quantify instability in terms of $S^2 - 4N^2$, where $S^2 = U_z^2 + V_z^2$ is the squared vertical shear of horizontal current and $N^2 = (-g/\rho)\partial\rho/\partial z$ is the squared buoyancy frequency. When $S^2 - 4N^2 > 0$, flow is unstable, equivalent to a gradient Richardson number $\mathrm{Ri} = N^2/S^2 < 1/4$. The benefit of using $S^2 - 4N^2$ is that it remains finite as S approaches zero.

By towing SurfOtter at $\sim 1\,\mathrm{m\,s^{-1}}$, we obtain a two-dimensional picture of the internal waves caused by instabilities. Unfortunately, we cannot accurately estimate the relevant horizontal scale of this picture. Although we will include scale bars in the appropriate figures to give some reference for the wavelengths of instabilities, the scale is uncertain given the variation in the near-surface, mixed layer, and ship velocities together with the assumption that the internal wave field is traveling in only one direction. The indicated scale will assume a constant 60° skew between our transects and the internal wave propagation. A full description is given in appendix A. All times are presented in the local time (LT) zone (UTC + 8).

3. Comparing diurnal warm layers in calm and moderate winds

Sea surface temperature (SST) increased by at least 0.5°C on three days during our 2019 campaign (Fig. 1). Using similar labeling employed by Hughes et al. (2020b), "calm" refers to 23 September (winds typically $< 2\,\mathrm{m\,s^{-1}}$), "moderate" for 22 September (winds $\sim 4\,\mathrm{m\,s^{-1}}$), and "mixed" for 10 September (fluctuating between calm and moderate). Cumulatively, SurfOtter recorded data for 12 days during the field campaign, but all other days were either too windy ($\gtrsim 6\,\mathrm{m\,s^{-1}}$), complicated by a transient rain layer, or only partly recorded.

On the calm day, the vertical temperature gradient T_z was $> 0.5°\mathrm{C\,m^{-1}}$ for 7 h (Fig. 1j). The resulting thin diurnal jet ($0.07\,\mathrm{m\,s^{-1}}$) was associated with $S^2 \approx 1 \times 10^{-3}\,\mathrm{s^{-2}}$ over the top 2 m (Fig. 1m). This would be large in many parts of the ocean; Weller and Price (1988), for example, observed near-surface shear this large in winds of $15\,\mathrm{m\,s^{-1}}$. Here, it is small in the sense that $S^2 < 4N^2$ (Fig. 1p). On the moderate day, S^2 was again approximately $1 \times 10^{-3}\,\mathrm{s^{-2}}$ (Fig. 1o), but the shear extended deeper than on the calm day. Of the three days, the largest shear ($S^2 \approx 5 \times 10^{-3}\,\mathrm{s^{-2}}$) occurred on the mixed day (middle column; Fig. 1). This is close to our predicted peak shear of $S^2 = 7 \times 10^{-3}\,\mathrm{s^{-2}}$ at a wind speed of $2\,\mathrm{m\,s^{-1}}$ in a one-dimensional model [presented as $S^2 \approx 0.08\,\mathrm{s^{-2}}$ in Fig. 11a in Hughes et al. (2020a)].

We interpreted the $2\,\mathrm{m\,s^{-1}}$ wind speed in this earlier study as a threshold above which $S^2 > 4N^2$. Below this wind speed, there is negligible shear-driven mixing, the diurnal jet remains thin, and its speed and shear increase with wind speed. Our observations here confirm the $2\,\mathrm{m\,s^{-1}}$ threshold prediction: $S^2 - 4N^2$ is negative on the calm day (Fig. 1p), positive near the surface on the moderate day (Fig. 1r), and changes sign on the mixed day (Fig. 1q) as wind speeds fluctuate about $2\,\mathrm{m\,s^{-1}}$.

We observe oscillations, as expected, when the flow is unstable ($S^2 - 4N^2 > 0$). Using a representative 10-min period (1700–1710 LT) on each of the three days, Fig. 2 shows oscillations of isotherms (here equivalent to isopycnals) of 1–2 m on the moderate day, but only a fraction of a meter on the calm day. Soloviev and Lukas (1997) made a similar observation: internal waves in the top 2 m occurred under 3–5 $\mathrm{m\,s^{-1}}$ winds but not $1\,\mathrm{m\,s^{-1}}$ winds (their Fig. 12).

To extend and quantify this representative period to the whole three days, we calculate the standard deviation of the depth of the isotherm corresponding to the depth- and time-averaged temperature in each 10-min block (e.g., the black contours in Fig. 2). We intend this as an ad hoc measure of the

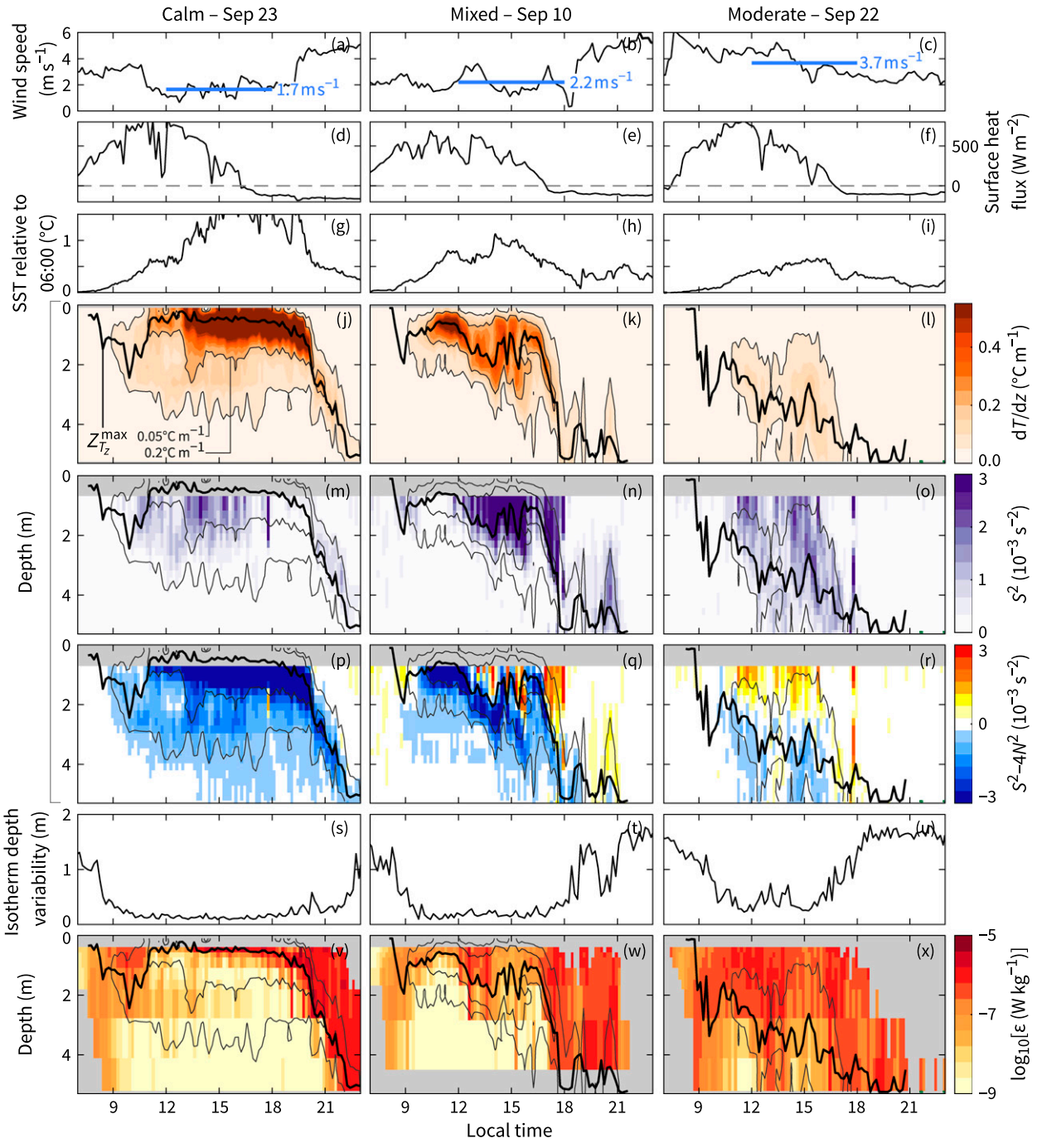

FIG. 1. Measured and derived parameters for the three DWLs measured in the 2019 field campaign. Mean wind speed from 1200 to 1800 LT is highlighted with a blue horizontal line and increases from (a) to (c). To aid interpretation for each day, we repeatedly include two temperature gradient contours and the depth of maximum temperature gradient $z_{T_z}^{\max}$ [see (j)]. The apparent outliers in (o) and (r) in S^2 at 1745 LT are associated with a band of strong shear that rose from 5 to 2 m and fell back in the space of 3 min.

prevalence of shear instabilities but recognize that it also incorporates convective instabilities at night. On all days, oscillations were small through much of the late morning and early afternoon: ~0.2 m on the calm and mixed days and 0.5 m on the moderate day (Figs. 1s–u). Oscillations increased later in the evening as conditions become more conducive to growth of instabilities (as will be discussed in section 5).

The final parameter we show is the turbulence dissipation rate ε (Figs. 1v–x). This is derived from 6–8 fast thermistors (100 Hz) using the method detailed by Hughes et al. (2020b).

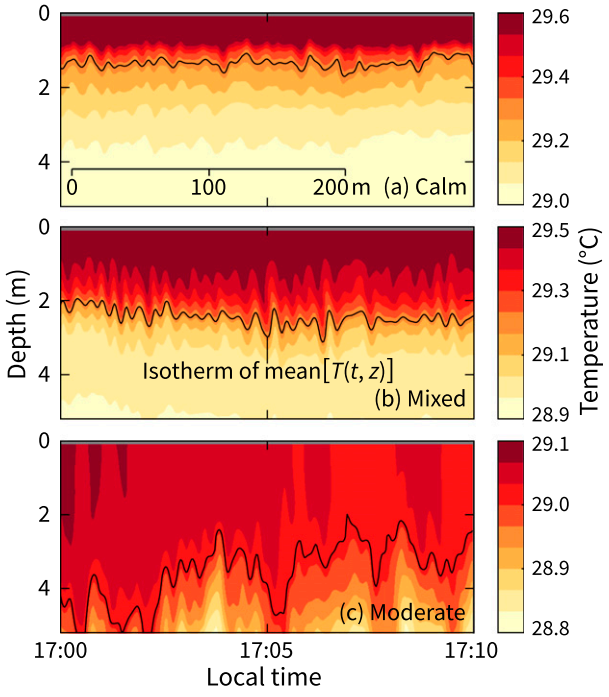

FIG. 2. Isotherm oscillations, presumed to be caused by shear instabilities, increase in size with wind speed. Note that the range of the color scale is smaller by a factor of 2 on the moderate day. See appendix A for details of the scale estimate.

As in that study, we find that the depth of maximum temperature gradient $z_{T_z}^{\max}$ separates the regions of large and small ε.

With measurements of ε, S^2, and N^2, we can estimate vertical eddy viscosity A_v and diffusivity K_v using conventional expressions (e.g., Osborn 1980). $K_v = \Gamma\epsilon/N^2$ and $A_v = (1+\Gamma)\epsilon/S^2$, where Γ is taken to be 0.2. On the calm, mixed, and moderate days, respectively, the median K_v values are 0.2, 0.6, and $7 \times 10^{-4}\,\mathrm{m^2\,s^{-1}}$, and the median A_v values are 0.6, 2, and $7 \times 10^{-4}\,\mathrm{m^2\,s^{-1}}$. As an example measure of spread, the middle 50% of the distributions of A_v and K_v both span approximately 2×10^{-4}–$20 \times 10^{-4}\,\mathrm{m^2\,s^{-1}}$ on the moderate day.

4. Diagnosing shear instability under moderate winds

We focus on the moderate day since the signature of shear instability is prevalent. On this day, the surface warms by 0.5°C relative to the temperature at 10 m (Fig. 3a), and the diurnal jet accelerates to $0.17\,\mathrm{m\,s^{-1}}$ by 1400 LT, close to the oft-quoted $0.15\,\mathrm{m\,s^{-1}}$ (e.g., Price et al. 1986). It moves downwind initially and then rotates inertially (Figs. 3b,c; see also Hughes et al. 2020a).

Temperature and velocity both increase toward the surface, but they do so differently. A velocity signal must originate at the surface due to wind stress, whereas a temperature signal originates from penetrating insolation, a depth-distributed heat source. We observe the largest shear in the top 2 m until 1500–1600 LT (Figs. 3d,e) indicating that the wind stress input at the surface is not efficiently transported downward. Conversely, the combined effect of surface heat loss, penetrating insolation, and mechanical mixing means that stratification peaks away from the surface (at 4 m deep at 1400–1500 LT, for example; Fig. 3e). Although one-half or more of the sunlight is absorbed in the top 1 m (e.g., Paulson and Simpson 1977), there may exist a convectively unstable surface region of thickness O(1–10) cm in which surface heat loss exceeds absorbed insolation (see section 6b).

Perhaps surprisingly, near the surface $S^2 \gg 4N^2$ (Ri $\approx$ 0.1) at 1400–1500 LT (Fig. 3e) despite the hour-long averaging. Indeed, reexamining Fig. 1r, we observe a region of unstable

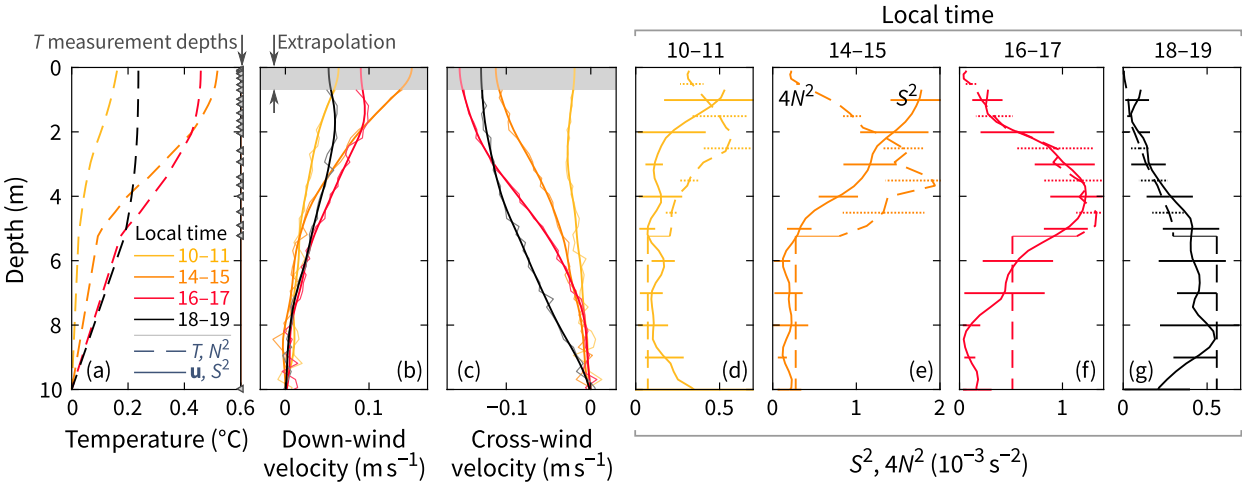

FIG. 3. Evidence of near-surface instability ($S^2 > 4N^2$) measured on the moderate day. (a)–(c) Representative hourly means of temperature and velocity relative to 10 m. (d)–(g) Shear and stratification derived from (a)–(c). SurfOtter temperature measurements only extend to 5.3 m. The reference measurement at 10 m comes from concurrent, repeat vertical profiling from the ship. Error bars at nominal depths span plus/minus the root-mean-square error of the six 10-min averages of S^2 and $4N^2$ within each hourly average. Extrapolation of velocity is discussed in section 4a.

flow persisting for several hours. By contrast, the profiles at 1600–1700 and 1800–1900 LT (Figs. 3f,g) demonstrate $S^2 \approx 4N^2$. The latter is a more familiar regime; Smyth et al. (2019), for example, compiled a list of observations of eight such marginally unstable flows covering a wide range of spatial scales.

A key difference between the profile starting at 1400 LT and those later is the location of the shear relative to the sea surface. This affects how quickly instabilities grow and therefore the rate at which shear is mixed away. To demonstrate, we first look in detail at instabilities predicted by the profiles from 1400 to 1500 LT and then artificially change the distance of the shear from the free surface. We employ this analysis in section 5 to relate diurnal changes in observed shear profiles to changes in growth rate.

a. Linear stability analysis of measured profiles

The initial, linear growth of a stratified shear instability can be diagnosed from the Taylor–Goldstein equation. This linear stability analysis (LSA) predicts the growth rate, wavelength, and vertical structure of the instability. For a thermally stratified fluid, instabilities are assumed to have vertical velocity and temperature perturbations (w', T') of the following form:

$$w' = \text{Real}[\hat{w}(z)\exp(\sigma t + ikx)] \quad \text{and} \tag{1}$$

$$T' = \text{Real}[\hat{T}(z)\exp(\sigma t + ikx)]. \tag{2}$$

In stable flow, neglecting molecular effects, σ is purely imaginary and the expressions reduce to traveling, sinusoidal internal waves with depth-dependent complex amplitudes of $\hat{w}$ and $\hat{T}$. In unstable flow $\sigma = \sigma_r + i\sigma_i$, with the positive real component being the growth rate of instabilities. It is the inverse time scale for a linear perturbation to grow by a factor of e.

For a given wavenumber k, $\hat{w}$ and $\hat{T}$ are eigenfunctions corresponding to the eigenvalue of σ. By solving the equation with many possible choices of k, we identify the mode expected to dominate after a finite amount of time. This is termed the fastest-growing mode (FGM).

We use a matrix method to solve the Taylor–Goldstein equation, extended to include viscosity and diffusion (which may be molecular or turbulent). Vertical discretization employs the Fourier–Galerkin method (Lian et al. 2020). The domain is 50 m deep and uses a constant 0.1-m grid spacing. This is deep enough to ensure the artificial "seafloor" has negligible effect on the solution while being shallow enough to allow for efficient computation. Viscosity and diffusivity in both the horizontal and vertical are set to $5 \times 10^{-5}\,\text{m}^2\,\text{s}^{-1}$. This is large enough to ensure that the growth rate does not increase without bound with increasing wavenumber (cf. Thorpe and Liu 2009) and yet small enough to comply with the notion of an instability developing within an initially quiescent, horizontally homogeneous fluid. Although this notion is seldom truly valid (Kaminski and Smyth 2019), it is a useful approximation here.

An instability is likely to grow most quickly in a direction parallel to that of maximum shear. Here, to a good approximation, this is also the direction of the diurnal jet itself as estimated from the velocity in the top 2 m. Therefore, we project the depth-varying vector velocity onto this direction to produce a velocity in one horizontal dimension. Below 10 m, velocity and temperature are extrapolated assuming zero shear and stratification. Because our shallowest velocity observation was 0.7 m, we must extrapolate profiles above this depth (shaded region in Figs. 3b,c). To do so, we assume that wind-, wave-, and buoyancy-driven turbulence combine in such a way that shear is zero at the surface and linearly increases with depth in the top 0.5 m. The effects of this choice are discussed in sections 4b and 6b.

For the profiles from 1400 to 1500 LT (Fig. 4a), we conduct the LSA for wavelengths between 10 and 200 m in increments of 3 m and find a maximum growth rate at 60 m (Fig. 4b). For this wavelength, we show the associated values of $|\hat{w}|$ and $|\hat{T}|$ (Fig. 4c), which depict the magnitude of variability in w and T as a function of depth.

To corroborate the LSA, we compare the result with a two-dimensional simulation with the MITgcm (Marshall et al. 1997; Adcroft et al. 2004) initialized with the same temperature and velocity profiles. We use a model grid that is 1000 m long and 500 m deep with 0.2-m grid spacing in the top 3 m and increasing by 3% per cell below. (This grid will be reused later to simulate a diurnal cycle, in which case it is necessary to use a deeper depth than that for the LSA.) Viscosity and diffusivity are the same as the LSA ($5 \times 10^{-5}\,\text{m}^2\,\text{s}^{-1}$). The simulation is nonhydrostatic, with a time step of 1 s, and a third-order flux limiter advection scheme for temperature. Random perturbations of ~0.001°C are added to the initial temperature field, which is otherwise horizontally homogeneous.

Waves approximately 60 m long grow over an hourly time scale (Fig. 4d) as predicted by the LSA. The shape of the root-mean-square vertical velocity and temperature anomalies also agrees with the LSA (Fig. 4e). The overall agreement between the two independent methods makes us confident that we have accurately diagnosed the behavior of the fastest-growing mode.

b. Distance of shear from sea surface controls the growth rate

For the fastest-growing mode identified in the previous section, "fast" is a relative term. The maximum growth rate predicted is $0.6\,\text{h}^{-1}$. By comparison, with shear that is an order of magnitude larger, growth rates in estuaries can reach $O(100)\,\text{h}^{-1}$ (Tedford et al. 2009). In some analyses, the $0.6\,\text{h}^{-1}$ value would fail a threshold test. Smyth et al. (2011), for example, discard values below $1\,\text{h}^{-1}$. Going below this threshold, we begin to invalidate the assumption used in LSA that instabilities evolve faster than the mean flow varies. Despite some possible inaccuracy, low growth rates are still meaningful here in giving a sense of the potential for growth or lack thereof.

The low growth rate arises because of the stabilizing influence of the sea surface. This can be seen by repeating the previous analysis, but artificially shifting the observed shear and stratification away from the surface. (The shift is in addition to the extrapolated decrease of shear in the top 0.5 m noted in section 4a.) A shift of 2–3 m increases the growth rate by a factor of 15 (from 0.6 to $9\,\text{h}^{-1}$; Fig. 5a). We emphasize that there is no change to the input temperature and velocity

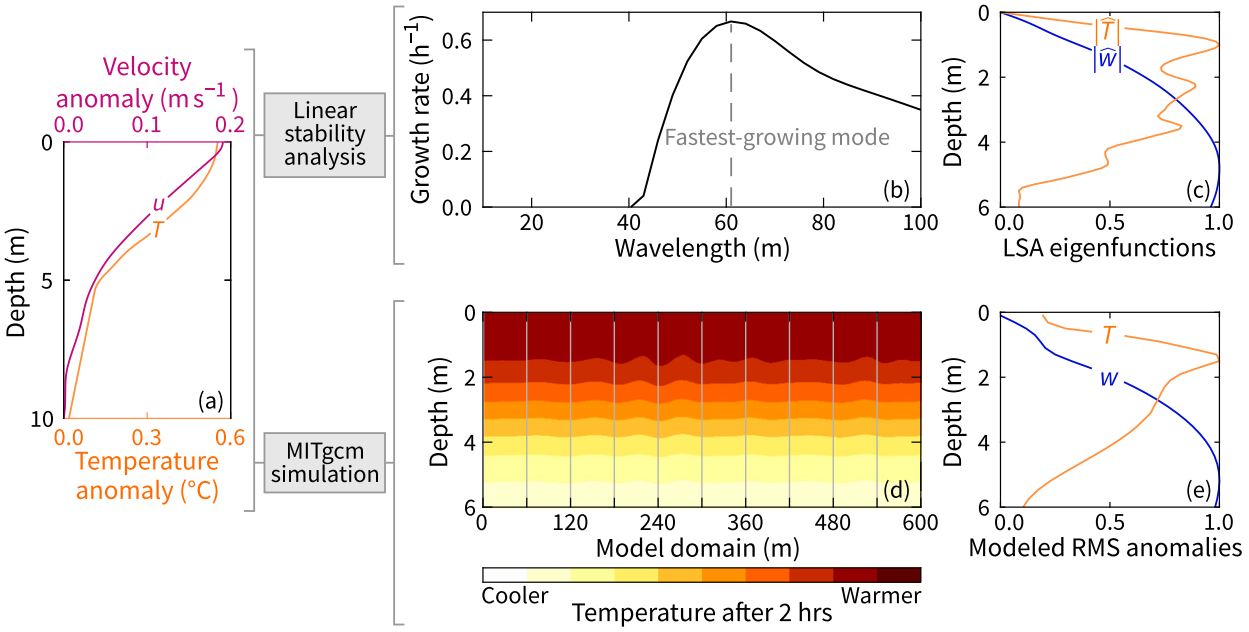

FIG. 4. Linear stability analysis for T and u profiles at 1400–1500 LT on the moderate day. Two distinct methods are used and compared: (top) numerical solution of a one-dimensional eigenvalue problem and (bottom) an MITgcm simulation initialized with T and u profiles. (a) Input profiles for both analyses. (b) The fastest-growing mode is identified via LSA for many wavelengths. (c) The absolute value of the eigenfunctions (normalized to their maxima) for the fastest-growing mode: vertical velocity w and temperature T. (d) The temperature field exhibits waves with wavelengths comparable to that for the fastest-growing mode in (b). Vertical isotherm displacements are doubled for clarity. (e) Quantities equivalent to (c), but derived from the model output in (d).

profiles except the vertical shift; both temperature and velocity are set as constant in the surface region (Figs. 5b,c). As will become clear, the velocity shift matters more than the temperature shift.

Consequences of increased growth rates are evident in snapshots of simulations using three representative shifts (0.0, 0.5, and 2.0 m; Figs. 5d–o). Whereas the simulation without a shift shows minimal growth even after 120 min, a shift of 2.0 m allows for an instability that overturns within 40 min. Alternatively, we repeated the zero-shift simulation but with constant shear in the top 0.5 m, rather than extrapolating to zero at the surface. In this case, there is no sign of instability even after 3 h. More generally, varying from 0 to 1 m the depth at which we impose the extrapolation to zero surface shear, we obtain growth rates of 0–2 h^{-1} (not shown). Ultimately, these results together highlight the role of a near-surface vorticity gradient in the development of instability (see section 6b).

5. Evolving behavior of the shear instabilities

a. Observed changes in instability

The analysis for the period 1400–1500 LT in the previous section serves to explain the qualitative behavior of the instabilities throughout much of the daylight part of the day. Snapshots of the temperature field every 2 h from 1000 to 1600 LT all display finite but modest isotherm displacements of ~1 m with wavelengths of ~50 m (Figs. 6k–n).

Isotherm displacements are larger before 1000 LT (Fig. 6j), but are more difficult to interpret because the temperature change across our 5 m measurement range is small (~0.02°C). As a reference, fields at 0600 LT (Figs. 6a,i) show the level of variability before the onset of daytime heating.

A different picture emerges in the evening (1800 and 2000 LT) with isotherm displacements often exceeding our 5 m measurement range. At 1800 LT, stratification is stable when averaged over 1 h, but shows signs of convective instability in the top 2 m on the 2-s scale (not shown). This convection is presumed sufficient to reduce the near-surface shear and move some of it downward far enough that the shear instabilities can grow more quickly. In other words, convection is not the direct cause of large isotherm displacements, but rather a catalyst for shear-driven instability.

Repeating the LSA described earlier for hourly averaged profiles throughout the day, we find that growth rates are small from 1000 to 1600 LT (Fig. 7c). Even the peak value of 2 h^{-1} at 1130 LT is small in absolute terms. After 1600 LT an abrupt increase in growth rate occurs (Fig. 7c). This coincides in time with the region of $S^2 > 4N^2$ moving from the top 2 m down below 2 m (Fig. 7b). The increase in growth rate of the FGM occurs despite a decrease in $S^2 - 4N^2$ (or equivalently an increase in Ri). Hence, the change is consistent with the influence of the shape of the shear profile near the surface as demonstrated in section 4b.

The maximum growth rate of 5 h^{-1} occurs for the 1730–1830 LT period. It then decreases as shear is effectively either mixed away or mixed downward. Indeed, Fig. 7 intentionally stops at 1900 LT because the diurnal thermocline is too deep thereafter for our measurements to allow an adequate LSA.

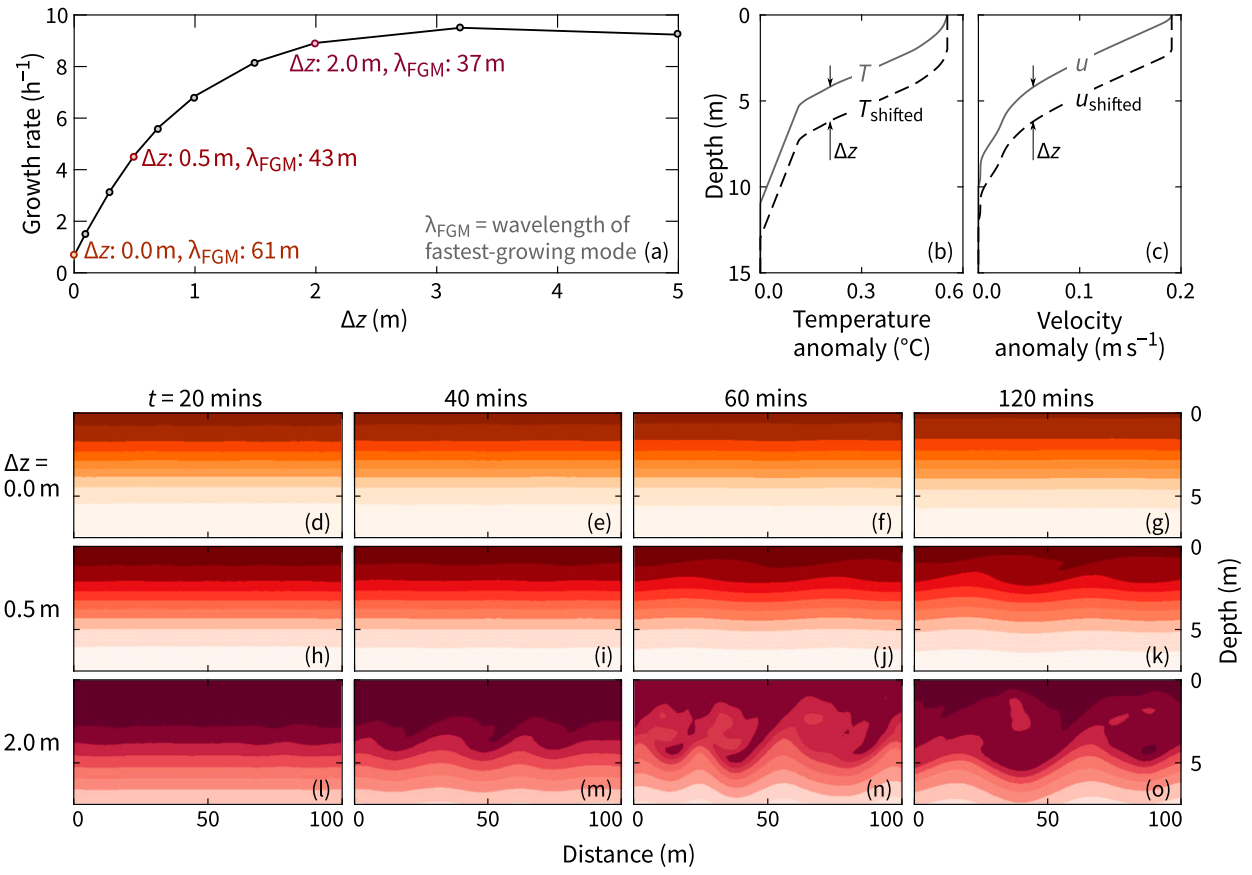

FIG. 5. Artificially shifting shear and stratification downward from the surface increases the instability's growth rate by an order of magnitude. (a) Growth rates predicted from LSA (see Fig. 4). (b),(c) Definition of the downward shift Δz. (d)–(o) Snapshots of the temperature field at four times from simulations using three representative Δz values.

A complementary picture of the likelihood of DWL instability throughout the day is given by Cronin and Kessler (2009), whose measurements of N^2 and S^2 cover 5–25 m.

b. *Simulated changes in instability*

Our observations of instability on the moderate day are limited in three ways. First, we have only a single realization of an entire day. Second, horizontal and temporal variability are not measured independently. Third, our measurements do not capture the full depth range of the DWL evolution. We address these issues by developing a second realization, a two-dimensional simulation of the full diurnal cycle of a DWL subject to moderate winds and diurnal heating (Fig. 8). Unlike those in section 4a, this simulation is not initialized with any observed temperature or velocity profiles. Instead, it is initialized at 0400 LT with a motionless, 60-m-deep mixed layer.

Much of the set up for the simulation is straightforward to implement: we use the same model grid described in section 4a (500 × 2-m grid cells horizontally and 500 m deep with 0.2-m resolution near the surface), we force with a constant wind speed of 4 m s^{-1}, and we apply diurnal heating that has zero net heat input on daily average (Fig. 8a). Penetrating solar radiation is treated with a nine-band formulation with a solar-angle dependence described by Gentemann et al. (2009). Because the grid is two-dimensional (x–z), we set Coriolis frequency f to zero rather than let the diurnal jet veer inertially throughout the day (e.g., Hughes et al. 2020a). This ensures the jet is always traveling in the direction in which instabilities can evolve. (Instabilities cannot occur in the y direction.) Although inertial turning can limit the speed ultimately attained by the jet (Price et al. 1986), the effect at our low latitude is small. Further, f is small relative to growth rates. Hence, the two-dimensional constraint is reasonable.

The parameters that will have the most influence on model output are the eddy viscosity A and eddy diffusivity K. These should be large enough to ensure the wind's momentum is mixed downward at a realistic rate, but not too large to preclude the shear instabilities that we aim to resolve. For simplicity, we set the background values of K and A to be equal to each other, isotropic, and spatially constant. We tuned this value such that the model reproduced the observed pattern and approximate magnitude of $S^2 - 4N^2$ as a function of time and depth (cf. Figs. 7b and 8b). Because approximately half of the solar energy is absorbed in the top 0.5 m, $S^2 - 4N^2 < 0$ over this depth (Fig. 8b). Our observations do

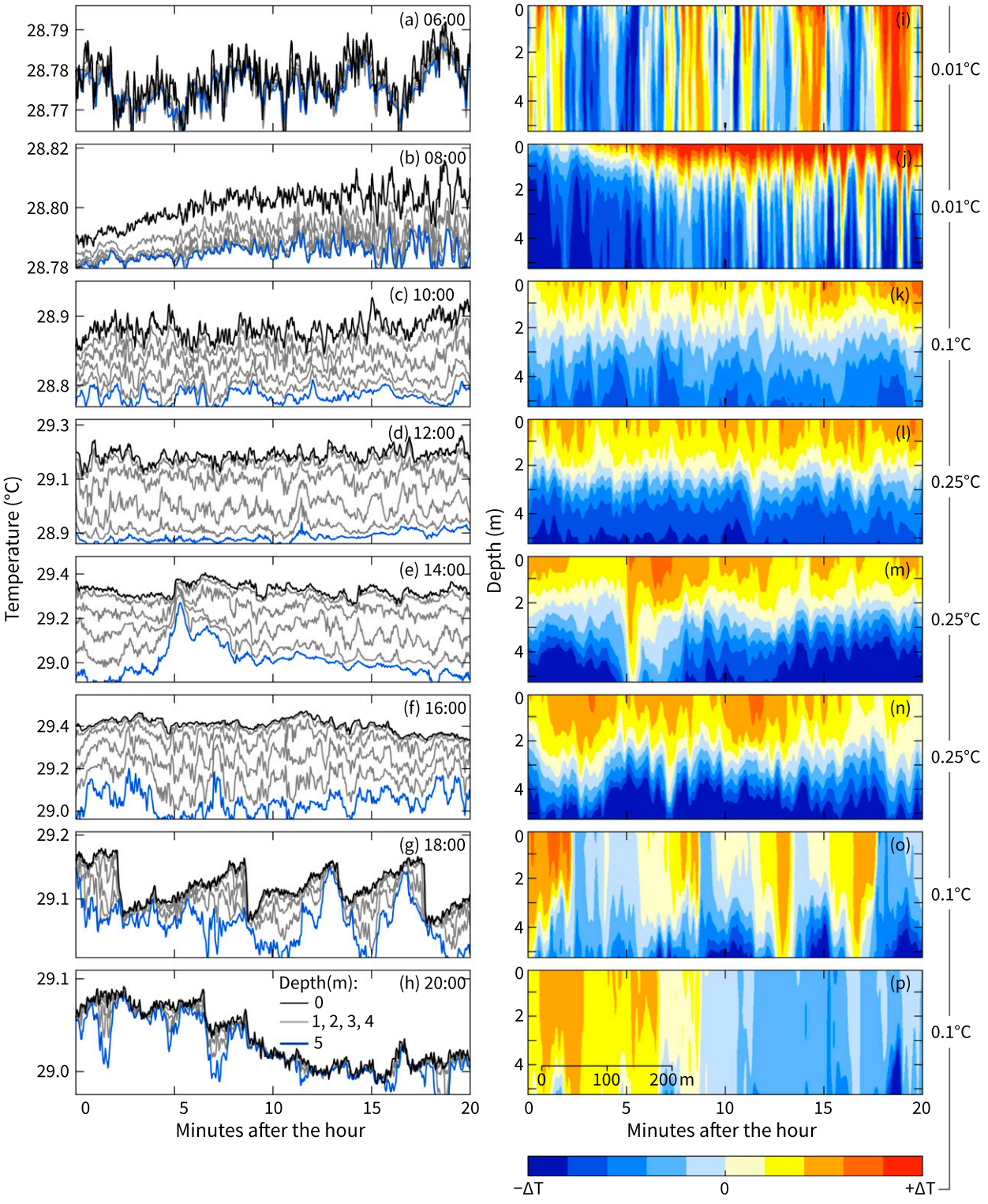

FIG. 6. Evolution of the temperature field on the moderate day. Time series are linearly interpolated to the evenly spaced levels shown. Contours show $T(z, t)$ relative to the depth- and time-averaged T over each 20-min period. The scale bar in (p), assumed to apply to all panels, should be considered uncertain as described in appendix A.

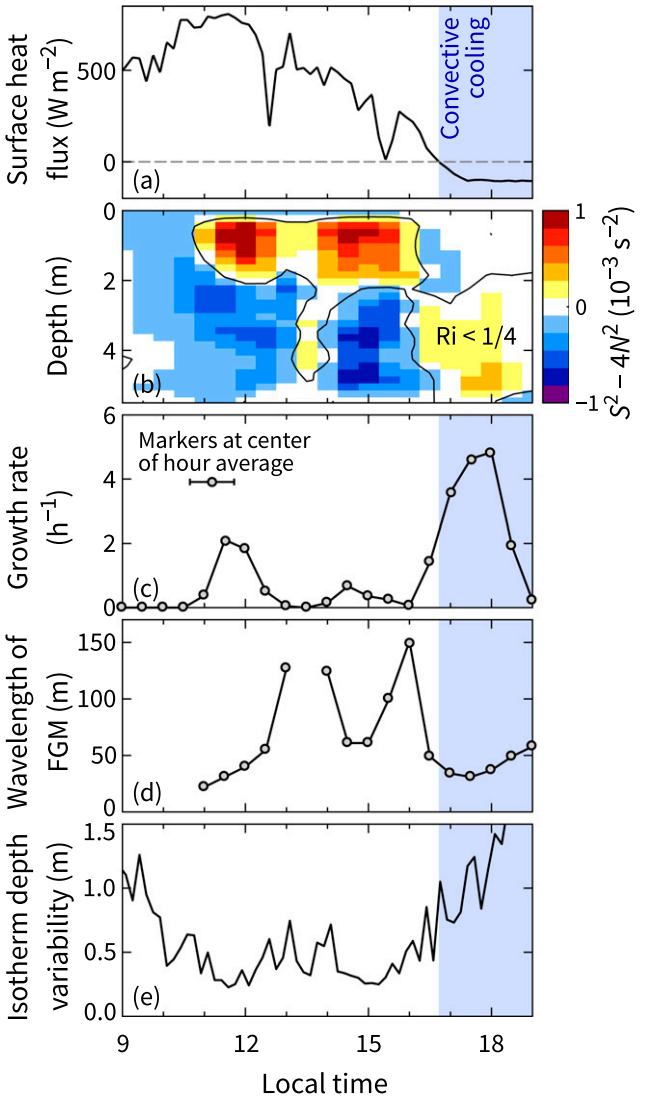

FIG. 7. A significant increase in the instability growth rates occurs when the unstable region moves away from the surface. An LSA is undertaken every 30 min from hourly averaged (i.e., half overlapping) profiles of density and velocity. The quantities in (a),(b), and (e) were shown in Fig. 1 and are repeated here for context, although a different color scale and averaging period is used for $S^2 - 4N^2$. Wavelengths of the FGM are not shown if the calculated growth rate is less than 0.02 h^{-1}.

not exhibit this near-surface increase in stratification on the moderate day (Fig. 1*l*), but it extends over only a small depth range, so we expect it to have minimal dynamical significance.

With much trial and error, we settled on a background value of $K = A = 3 \times 10^{-4}\,\mathrm{m^2\,s^{-1}}$. (Significant changes in $S^2 - 4N^2$ occur if this value is varied by more than ±50%.) We increase K and A in regions of convective instability to $K = A = 1 \times 10^{-2}\,\mathrm{m^2\,s^{-1}}$. This parameterizes the three-dimensional turbulence that results from convective cooling and any shear-generated overturns. Between 1200 and 1600 LT, K and A increase in 3%–6% of grid points between 1 and 5 m deep as small overturns occurs. This reaches 50% at 1800 LT as both shear- and convectively generated overturns occur.

Overall, the simulation qualitatively reproduces the observed temperature fields as a function of time of day (Figs. 8c–j), with the added benefit of better estimates of the vertical and horizontal scales of the instabilities. Between 1000 and 1600 LT, $S^2 - 4N^2 \approx 2 \times 10^{-3}\,\mathrm{s^{-2}}$ and instabilities are visible, but typical isotherm depth variability is only $O(1)$ m. This increases to $O(5)$ m by 1800 LT. Overturning of the waves, together with

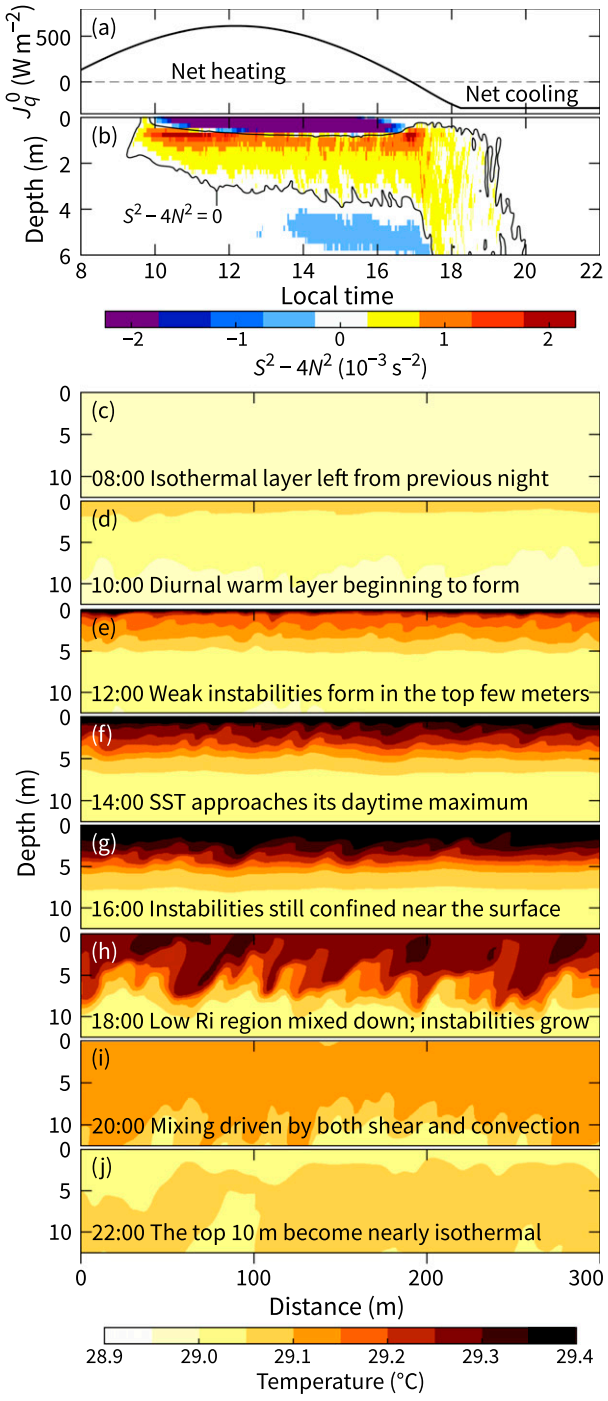

FIG. 8. A simulated DWL that reproduces much of the observed behavior. Note, in particular, the increase in size of the instabilities after the onset of convective cooling in the evening [cf. (g) and (h)].

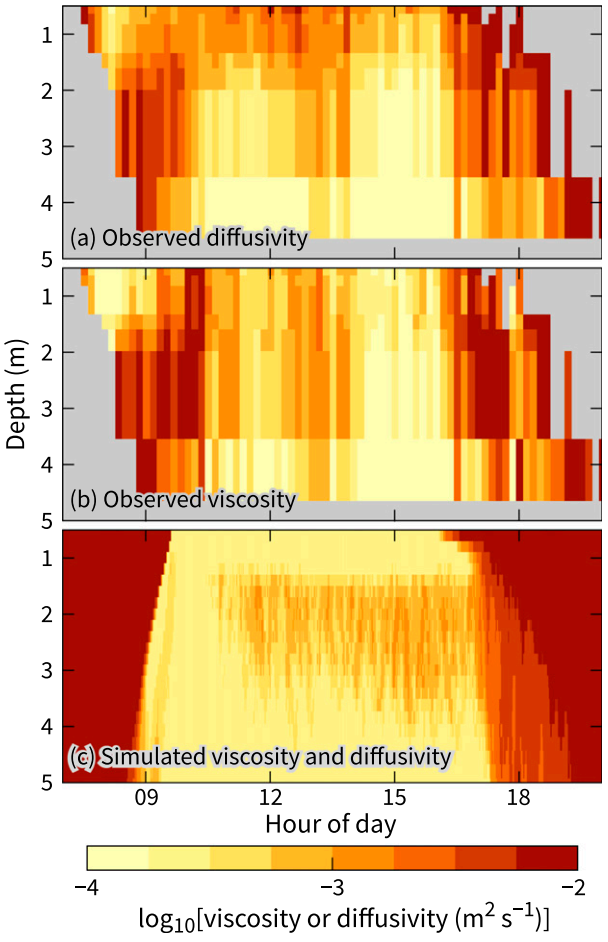

FIG. 9. A comparison of the observed eddy mixing coefficients on the moderate day with those from the diurnal simulation. Observed values are derived from ε, N^2, and S^2 (section 3). In the simulation, viscosity and diffusivity are equal. In any given grid cell, their value is either 3×10^{-4} or 1×10^{-2} m^2 s^{-1}. Values between this range arise from averaging horizontally across the domain.

surface-driven convection, mixes away much of the excess shear. After 1900 LT, $S^2 - 4N^2 \approx 0$.

We also compare the simulation with observations in terms of eddy mixing coefficients. This is partly a test of model behavior and partly a demonstration after the fact that our mixing scheme is reasonable. Figures 9a and 9b show the diffusivity and viscosity derived, where possible, from the observed ε, N^2, and S^2 (section 3). In the simulation, the two coefficients are set equal to each other and are shown in Fig. 9c as a horizontal average. The observed and simulated values agree on the first-order pattern with values $\lesssim 10^{-3}$ m^2 s^{-1} in the middle of the day and larger values earlier and later. There is less agreement at second order, but we would not expect this level of agreement given that the simulation is subject to idealized insolation and winds rather than the observed forcing.

6. Discussion

a. *Broad classifications of the instabilities*

The stratified shear instabilities that we have observed here exist on a continuum between two end members: those earlier

in the day during the heating period and those in the evening around the onset of convective cooling. We address the latter first.

At approximately 1630 LT on the moderate day, there is an abrupt decrease in the near-surface stratification (Fig. 1l) indicating increased mixing. Two related changes occur around this time: an increase in growth rate (Fig. 7c) and the vertical alignment of density and velocity interfaces (Figs. 3f,g). With this alignment, the similar thicknesses of the two interfaces means that Kelvin–Helmholtz instability is likely as the thickness ratio is the primary nondimensional parameter governing the type of instability in this case (e.g., Alexakis 2005). We confirmed the presence of Kelvin–Helmholtz instability using a simulation like that shown in Figs. 5d–5g, but initialized with velocity and density from 1730 to 1830 LT. In this simulation (not shown), billows appear after 1 h as would be expected for a growth rate of $5\,\mathrm{h}^{-1}$ as in Fig. 7c. At this same time of day, we see ramps in the measured temperature field (Fig. 6g), which are signatures of KH billows (Thorpe 1978). Overturning structures are also visible in the snapshot at 1800 LT from the full-day simulation (Fig. 8h). Moulin et al. (2018) inferred the same result about ramps and showed that they are most common 1.5 h before the surface heat flux changes to net cooling in the evening. In quantifying ramps, however, they required a minimum temperature gradient of $0.02^{\circ}\mathrm{C\,m}^{-1}$ and therefore underestimated the presence of ramps later in the evening.

Earlier in the day, the influence of boundary proximity is so dominant that the standard distinctions between Kelvin–Helmholtz, Holmboe, and asymmetric Holmboe instabilities are not informative. In the following section, we investigate why instabilities in general are hindered by a boundary.

b. *The role of vorticity gradients*

Kelvin–Helmholtz and Holmboe instabilities both involve the interaction of a vorticity wave with a second wave (Baines and Mitsudera 1994), either another vorticity wave (Kelvin–Helmholtz instability) or an internal gravity wave (Holmboe instability). As noted in section 4b, instability in a DWL depends on the presence of a vorticity gradient, or equivalently a vorticity wave, near the surface.

A vorticity wave is most easily understood in terms of a piecewise linear background velocity profile. In this case, the background vorticity gradient ($\partial^2 U/\partial z^2$) simplifies to a Dirac delta function at the interface of two pieces. This interface plays the same role that a density interface plays for an internal gravity wave in a two-layer fluid. In either case, a wave can propagate along the interface (see chapter 3 of Smyth and Carpenter 2019).

Consider the velocity profile at 1400–1500 LT including the extrapolated region (Figs. 3b,c). If we were to idealize this as a constant velocity layer above a constant shear layer, then the vorticity interface would be < 1 m from the sea surface. In similar bounded problems, this proximity to the boundary results in a reduced growth rate and a shift toward longer waves being destabilized (Hazel 1972; Pollard et al. 1972).

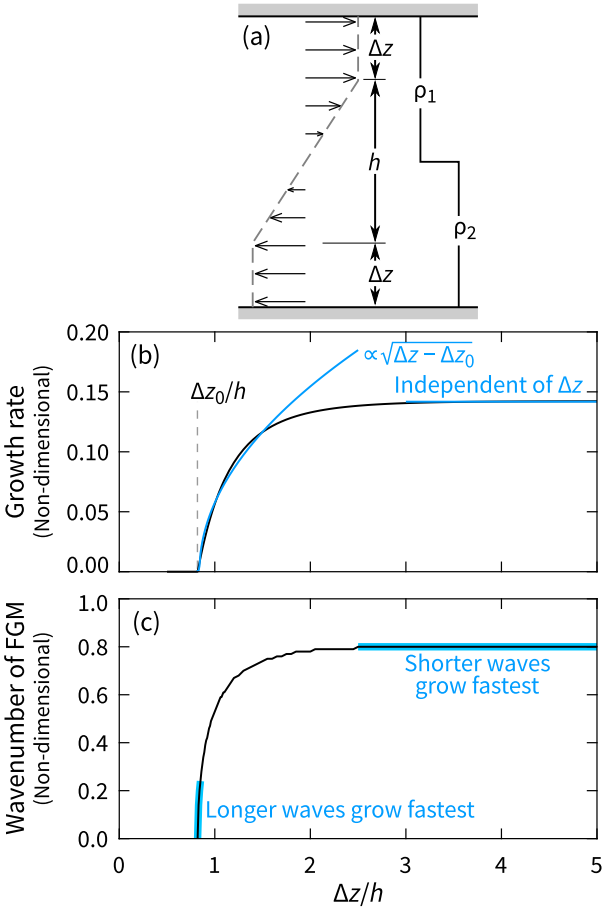

FIG. 10. The stabilizing influence of boundaries in an idealized instability. (a) The bounded, piecewise system that allows for an analytical solution for the instability (Haigh and Lawrence 1999). (b) The increase in growth rate with increasing Δz, which is the thickness of the unsheared regions, or equivalently the distance between the boundaries and the vorticity interfaces as shown in (a). (c) The wavenumber of the fastest-growing mode. The maximum values in (b) and (c) depend on the bulk Richardson number, which we have set here to 0.2. The additional blue curves denote the two limits discussed in the text.

To demonstrate, we will follow the analytical formulation[1] from Haigh and Lawrence (1999). They assume a piecewise linear velocity profile: a sheared layer between two finite-thickness unsheared layers; solid boundaries exist at the top and bottom (Fig. 10a). They allow for a vertical offset, but here we set the interface of the two-layer density profile at the center. The distance between each boundary and adjacent vorticity interface is denoted Δz to recognize its similar role to Δz in Fig. 5.

For Δz less than a certain thickness denoted Δz_0, the flow is stable (Fig. 10b). Just beyond Δz_0, the growth rate approximately

[1] The definition of $\gamma_{\pm}$ given by Haigh and Lawrence (1999) is missing a third $\pm$ sign. It should be $\gamma_{\pm} = (1 + 2\alpha)^2 \pm e^{4\alpha} \pm e^{2\alpha H}[(1 - 2\alpha)^2 \pm e^{-4\alpha}]$. This can be seen by comparison with the expressions in appendix A in Haigh (1995).

increases with the square root of the additional distance. For large Δz, the growth rate approaches a constant. (Similar limits arise in Fig. 5a for the observed profiles with artificial downshifts away from the sea surface.) Matching the growth rate curve in Fig. 10b, the associated wavenumber of the fastest-growing mode also increases quickly for $\Delta z \gtrsim \Delta z_0$ and approaches a constant thereafter (Fig. 10c). Put another way, comparing Figs. 10b and 10c demonstrates that when growth rates are low, longer waves are most unstable. This holds true for the observed instabilities. For example, Figs. 7c and 7d show that the slower-growing instabilities are those with wavelengths > 100 m whereas faster-growing instabilities have wavelengths of 30–50 m.

In section 4a, we imposed a low-shear region in the top 0.5 m, and therefore a vorticity interface in that vicinity, but only briefly proposed a cause. On one hand, our assumption seems reasonable: if turbulence is large near the surface, it will mix away shear. On the other hand, near-surface shear could be large owing to wind being its source at the surface (e.g., Csanady 1997). We have shown that a near-surface shear maximum is not maintained in the evening (Fig. 3g), when there is surface cooling and hence near-surface convective mixing. Such mixing can also occur to a lesser extent during net heating. Because the absorption of sunlight is distributed in depth, there is a shallow surface layer in which the net surface cooling overcomes the heating by locally absorbed insolation. The base of this layer at the "thermal compensation depth" varies from $O(0.01)$ m to $O(1)$ m depending on the surface cooling, depth-dependence of solar absorption, and time of day (e.g., Woods 1980). If wave-driven mixing and Langmuir circulation are negligible, then this depth may be a better estimate of the range over which to impose a low-shear region, rather than the 0.5 m value that we used. An associated uncertainty arises in the calculated growth rates before 1600 LT (Fig. 7c). Indeed, it is plausible that the tripling in isopycnal depth variability between 1200 and 1300 LT (Fig. 7e) is triggered by the cloud-induced decrease in surface heat flux at 1230 LT (Fig. 7a), which deepens the thermal compensation depth and hence alters the shear profile.

c. *Marginal instability?*

This section's title borrows from Thorpe and Liu (2009) because we readdress the same question: is the near-surface flow marginally unstable? Briefly, marginal instability arises when an unstable flow induces instabilities that grow nonlinearly and lead to enhanced turbulence, which then mixes the flow toward the critical Ri (see Smyth et al. 2019). Thorpe and Liu (2009) quantify the concept with the parameter φ, defined such that multiplying velocity by $1 + \phi$ is sufficient to stabilize the flow. In cases in which $\frac{1}{4}$ is the critical Ri, as it is here (appendix B),

$$\phi = -1 + \sqrt{4\mathrm{Ri}} = -1 + \sqrt{4N^2/S^2}.$$

In any unstable flow, ϕ is between -1 and 0. In marginally unstable flows, ϕ is close to zero. In their near-surface flow, Thorpe and Liu (2009) found that ϕ is not close to zero (-0.78) and they term the flow relatively unstable. For late morning and early afternoon, we find that $\phi \approx -0.4$, which is not close to zero since $S^2 \gg 4N^2$ near the surface. The low instability growth rate undermines marginal instability by limiting the turbulence generation step. Similarly, in the simulated day, $S^2 \gg 4N^2$in the late morning and afternoon, yet the instabilities are comparatively small (Figs. 8e–g). Consequently, the diurnal thermocline is slow to mix downward. Conversely, ϕ is close to zero after 1600 LT and the flow is marginally unstable ($S^2 \approx 4N^2$). It is after this time that the growth rate increases (Fig. 7c) and the mechanism underlying marginal instability thereby becomes effective.

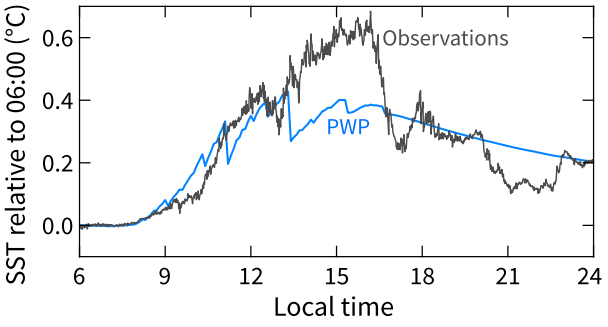

FIG. 11. SST during the afternoon is underpredicted by the PWP model (Price et al. 1986) because the parameterized near-surface mixing, a function of Ri, is too strong. Model forcing follows from the winds and surface heat flux presented in Figs. 1c and 1f.

d. *Implications for numerical modeling*

The concept of marginal instability, or more generally Ri-dependent mixing, is incorporated into many ocean models. The PWP model (Price et al. 1986), for example, calculates a mixed layer thickness with a critical bulk Ri of 0.65 and a transition layer below with a critical gradient Ri of 0.25. This model is relevant here because a simplified version of it is used to calculate warm layer corrections to subsurface temperature measurements for air–sea interactions (Fairall et al. 1996). Because our observed flow is not marginally unstable for part of the day, PWP will overestimate mixing at these times, and therefore underestimate SST. Indeed, it is between 1300 and 1600 LT that we observe the largest discrepancy between observed SST and that predicted by PWP forced by observed winds and heat fluxes (Fig. 11). Over this 3-h period, Gentemann et al. (2009) show that the Fairall et al. (1996) model underpredicts observed SST by 0.2°–0.3°C when averaged over 72 days with a diurnal warming signal.

At the other end of the modeling spectrum are large-eddy simulations (LES). Ideally, such models do not require any tuning of the mixing parameters. However, they do have a subtle, potential limitation related to their domain size. Recent simulations of DWLs use grid domains with horizontal dimensions of 64–256 m (Van Roekel et al. 2018; Sarkar and Pham 2019; Ushijima and Yoshikawa 2019). The larger end of this range may be sufficient, but the smaller end will constrain instabilities that we have shown are $O(50)$ m (Fig. 7d). With cyclic boundary conditions, waves that are not an integer divisor of the domain width will be inhibited. Another limitation of LES is the computing expense, especially given the need for grids approaching centimeter scales to accurately capture strongly stratified turbulence.

Two-dimensional simulations of DWLs with intermediate resolution are a good choice for future efforts looking to

cover a wide parameter space. (Adding a second horizontal dimension will be necessary when Coriolis frequency is too large to ignore or if winds veer significantly.) While we have shown that a two-dimensional simulation with idealized forcing can reproduce much of the observed qualitative behavior, we have not investigated changes in wind speed, surface heat flux, temporal variability of this forcing, Prandtl number, solar absorption profile, or mixed layer depth. This last parameter may change the nature of the instabilities by allowing wave energy to efficiently radiate downward (Smyth and Moum 2002; Pham and Sarkar 2014).

Our two-dimensional simulation was made possible by tuning against SurfOtter measurements of shear and stratification. This observation-informed model enables a realistic depiction of instabilities in a diurnal warm layer as they evolve in time in two dimensions. It is best appreciated as an animation created from snapshots output every minute (https://doi.org/10.5281/zenodo.4306935).

Acknowledgments. This work is part of the PISTON project funded by the Office of Naval Research. Partial funding is provided by NSF Grant OCE1851520. Engineers Kerry Latham, Pavan Vutukur, and Josh Logan helped to construct and maintain SurfOtter and the instruments it housed. Thanks are given to Elizabeth Thompson (NOAA Earth System Research Laboratory) for providing quality-controlled wind and heat flux data and to Roger Samelson for useful suggestions. Comments from Jeff Carpenter and an anonymous reviewer helped to improve several aspects of this paper.

Data availability statement. SurfOtter measurements for all three days discussed here, together with outputs for both the simulated day and the LSAs, are available at either https://doi.org/10.5281/zenodo.4306931 or kghughes.com/data. Matlab code for solving the viscous Taylor–Goldstein equation is available at http://blogs.oregonstate.edu/salty/matlab-tools-to-solve-the-viscous-taylor-goldstein-equation-for-both-instabilities-and-waves/.

APPENDIX A

Direction of Jet and Waves Relative to Our Transit

An ideal transit configuration in this study would have been one that moved perpendicular to wavefronts of the internal waves being analyzed. This equates to a transit parallel to the diurnal jet if we assume wavefronts are horizontally one-dimensional and perpendicular to the jet. Unfortunately, rather than parallel with the jet, our transects were closer to perpendicular. Here we describe how we estimate this relative angle between the transit and jet on the moderate day. An equivalent analysis for the two other days was undertaken but not shown.

Between 0900 and 2000 LT, we transited in a narrow ellipse 22-km-long aligned approximately north–south. Throughout the day the wind was toward the northeast (Fig. A1a). Using the measured wind, we can predict the direction of the diurnal jet by assuming it accelerates downwind initially and turns inertially thereafter. The angle α by which the jet turns follows from Hughes et al. (2020a):

$$\alpha = \tan^{-1}\left[\frac{\cos(ft) - 1}{\sin(ft)}\right], \tag{A1}$$

where f is Coriolis frequency and t is time relative to the formation of the diurnal warm layer (taken to be 0800 LT). Figure A1b shows the wind vectors rotated by α. Note the increasing rightward turning of the arrows in Fig. Alb relative to Fig. A1a with increasing time of day. (Before rotation, the wind at a given time is taken to be the vector-mean wind between 0800 LT and the given time.)

The direction of the diurnal jet can also be estimated directly from velocity observations. Here we do that by calculating the velocity in the top 2 m relative to the velocity at 10 m, which is assumed to represent the bulk mixed layer velocity. The observed jet direction (Fig. A1c) is typically within 10–20° of the rotated wind direction (not shown), with a maximum difference of 40°.

The jet's velocity is superimposed on that of the mixed layer. Because the mixed layer is much deeper, it acts to advect the jet as a whole. The alternative interpretation used here is to subtract the mixed layer velocity from the ship's transit velocity. For example, if the ship moves northward at 1.0 m s^{-1} into a southward current of 0.5 m s^{-1}, then the ship is effectively traveling at 1.5 m s^{-1} relative to the mixed layer.

The mixed layer current is estimated from velocities at 10–20 m deep from a 300-kHz ADCP. On this day, it was typically toward the northwest and 0.3–0.4 m s^{-1} but was smaller in the morning and late evening (Fig. A1d). The vector combination of ship transit velocity and mixed layer current is shown in Fig. A1e.

A comparison of the jet velocity with the combined ship and mixed layer current velocity shows that the two are nearly always closer to perpendicular than parallel (Fig. A1g). Note that Fig. A1f shows only the comparison with the directly observed jet direction, but Fig. A1g additionally shows the comparison using the rotated wind vectors. Although these two angle time series are broadly similar, they suggest an uncertainty that becomes problematic: the projection of the observed distance onto the jet's frame of reference involves a factor of $1/\cos(\theta)$, where θ is the angle in question. This factor grows without bound as θ approaches 90° (perpendicular).

Given all the challenges, and the questionable assumption that wavefronts are one-dimensional and perpendicular to the jet, we choose to make a large simplification with regard to the angle θ: we will assume θ is constant throughout the day ($\theta = 60°$, so $1/\cos\theta = 2$). In doing so, we acknowledge that any estimates of wavelengths are crude.

APPENDIX B

Stability Boundary for an Afternoon Profile

A requirement for instability is that $\mathrm{Ri} < 1/4$ somewhere in the flow. Yet this does not guarantee instability. As Hazel (1972) demonstrates, for example, the presence of boundaries

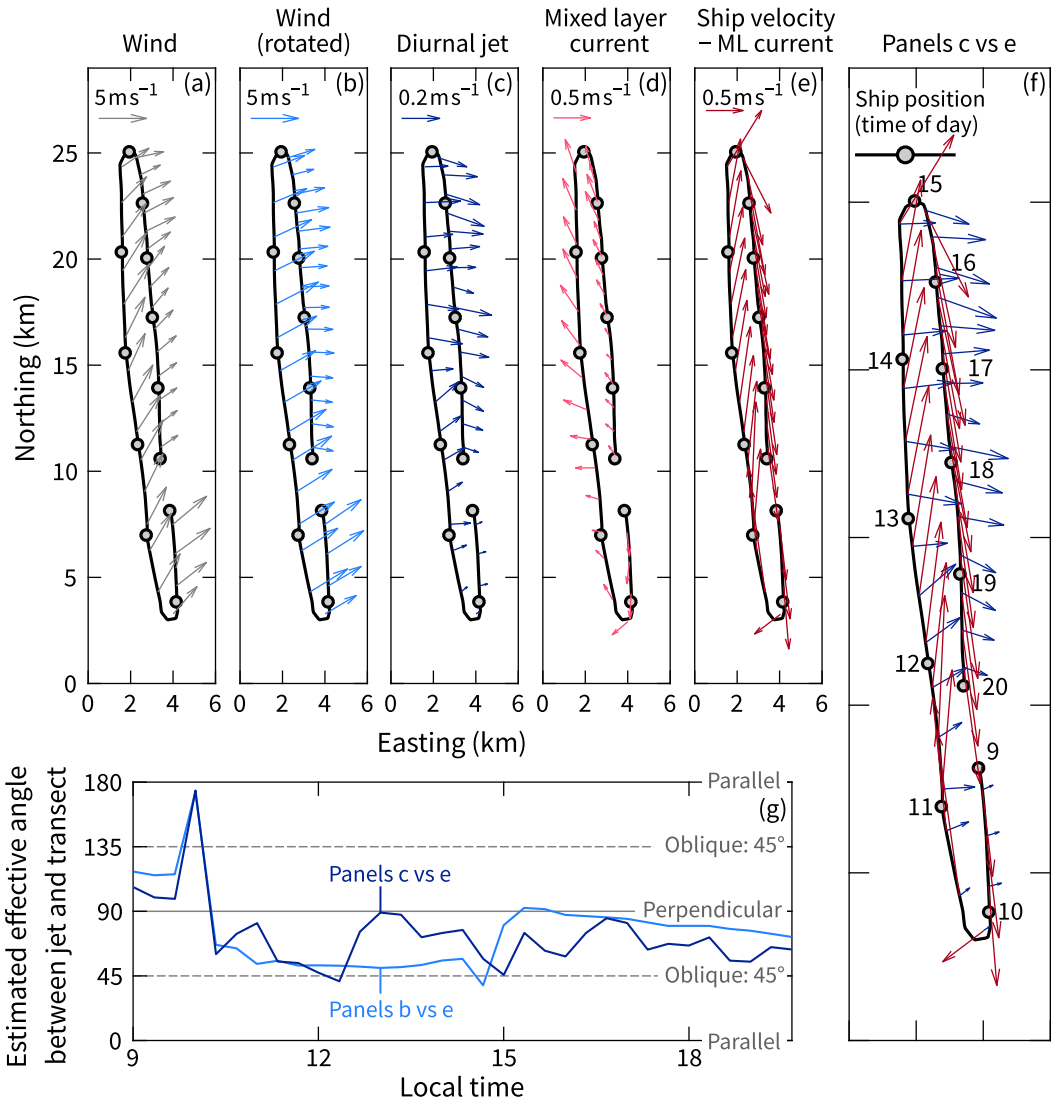

FIG. A1. Calculation of the relative angle between the diurnal jet and the ship's transit on the moderate day (22 September 2019). All arrows represent a certain velocity averaged in 20-min blocks and placed on a map of the ship's position between 0900 and 2000 LT. The location of (0, 0) in the maps is arbitrary. Note that the rotated wind vectors act as an inferred direction of the diurnal jet as described in the text.

can reduce the critical Ri, denoted Ri_c, below its otherwise standard value of 1/4. Nevertheless, he also notes that $\mathrm{Ri} < 1/4$ is quite a good ad hoc sufficiency criterion for instability in field measurements.

To determine the actual Ri_c for a given set of density and velocity profiles requires an LSA spanning multiple scenarios. In idealized cases, this is often presented as contours of growth rates versus nondimensional wavenumber and bulk Richardson number. Here we will present the contours versus wavelength and min(Ri), the minimum Richardson number within the given depth profile. We alter min(Ri) by multiplying the velocity profile by a factor of $1 + \phi$ (with ϕ being negative) following Thorpe and Liu (2009). As min(Ri) increases, the maximum growth rate reduces toward zero. The zero growth-rate contour is then the so-called stability boundary.

The stability boundary for the profiles at 1400–1500 LT on the moderate day indicates that Ri_c is, for our purposes, 1/4 (Fig. B1). We cannot confirm it is exactly 1/4 because we are relying on a numerical method to determine the growth rate. For example, applying our same method to conventional tanh profiles of density and velocity can give $\mathrm{Ri}_c \approx 0.26$ when the interfaces are thin. This is 0.01 above the known value (e.g., Hazel 1972) and the same value we see in Fig. B1. Further, to minimize numerical issues as the growth rate approaches zero, we use a viscosity and diffusivity of $10 \times 10^{-5}\,\mathrm{m^2\,s^{-1}}$ rather than the $5 \times 10^{-5}\,\mathrm{m^2\,s^{-1}}$ used elsewhere in the paper.

The 1400–1500 LT period is typical of much of the daytime in terms of its shear and stratification profiles (Figs. 1l and 1o). We therefore expect that $\mathrm{Ri}_c = 1/4$ throughout the moderate day. Further, once the region of low Ri moves away from the

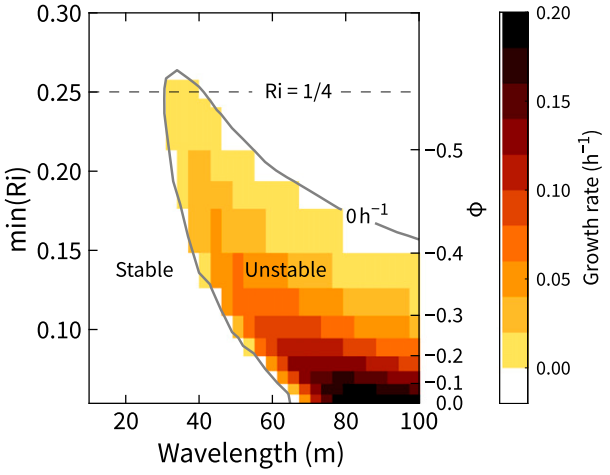

FIG. B1. The numerically derived stability boundary for the velocity and density profiles at 1400–1500 LT on the moderate day (see Fig. 3). The original profile, which corresponds to $\phi = 0$, has a minimum Ri of 0.06 at a depth of 0.5 m. The input velocity is increasingly reduced by multiplying the original profile by $1 + \phi$. Consequently, the minimum Ri increases as ϕ becomes more negative.

surface in the evening, the sea surface has less of an influence and there is less reason to suspect that $\mathrm{Ri}_c \neq 1/4$.

REFERENCES

Adcroft, A., C. Hill, J.-M. Campin, J. Marshall, and P. Heimbach, 2004: Overview of the formulation and numerics of the MIT GCM. *Proc. Seminar on Recent Developments in Numerical Methods for Atmospheric and Ocean Modelling*, Reading, United Kingdom, ECMWF, 139–149, https://www.ecmwf.int/node/7642.

Alexakis, A., 2005: On Holmboe's instability for smooth shear and density profiles. *Phys. Fluids*, **17**, 084103, https://doi.org/10.1063/1.2001567.

Antenucci, J. P., and J. Imberger, 2001: On internal waves near the high-frequency limit in an enclosed basin. *J. Geophys. Res.*, **106**, 22 465–22 474, https://doi.org/10.1029/2000JC000465.

Baines, P. G., and H. Mitsudera, 1994: On the mechanism of shear flow instabilities. *J. Fluid Mech.*, **276**, 327–342, https://doi.org/10.1017/S0022112094002582.

Carpenter, J. R., N. J. Balmforth, and G. A. Lawrence, 2010: Identifying unstable modes in stratified shear layers. *Phys. Fluids*, **22**, 054104, https://doi.org/10.1063/1.3379845.

——, E. W. Tedford, E. Heifetz, and G. A. Lawrence, 2013: Instability in stratified shear flow: Review of a physical interpretation based on interacting waves. *Appl. Mech. Rev.*, **64**, 060801, https://doi.org/10.1115/1.4007909.

Caulfield, C., 2021: Layering, instabilities, and mixing in turbulent stratified flows. *Annu. Rev. Fluid Mech.*, **53**, 113–145, https://doi.org/10.1146/annurev-fluid-042320-100458.

Cronin, M. F., and W. S. Kessler, 2009: Near-surface shear flow in the tropical Pacific cold tongue front. *J. Phys. Oceanogr.*, **39**, 1200–1215, https://doi.org/10.1175/2008JPO4064.1.

Csanady, G. T., 1997: The "slip law" of the free surface. *J. Oceanogr.*, **53**, 67–80, https://doi.org/10.1007/BF02700750.

Fairall, C. W., E. F. Bradley, J. S. Godfrey, G. A. Wick, J. B. Edson, and G. S. Young, 1996: Cool-skin and warm-layer effects on sea surface temperature. *J. Geophys. Res.*, **101**, 1295–1308, https://doi.org/10.1029/95JC03190.

Gentemann, C. L., P. J. Minnett, and B. Ward, 2009: Profiles of ocean surface heating (POSH): A new model of upper ocean diurnal warming. *J. Geophys. Res.*, **114**, C07017, https://doi.org/10.1029/2008JC004825..

Gímez-Giraldo, A., J. Imberger, J. P. Antenucci, and P. S. Yeates, 2008: Wind-shear-generated high-frequency internal waves as precursors to mixing in a stratified lake. *Limnol. Oceanogr.*, **53**, 354–367, https://doi.org/10.4319/lo.2008.53.1.0354.

Haigh, S. P., 1995: Non-symmetric Holmboe waves. Ph.D. thesis, University of British Columbia, 179 pp., https://doi.org/10.14288/1.0080013.

——, and G. A. Lawrence, 1999: Symmetric and nonsymmetric Holmboe instabilities in an inviscid flow. *Phys. Fluids*, **11**, 1459–1468, https://doi.org/10.1063/1.870009.

Hazel, P., 1972: Numerical studies of the stability of inviscid stratified shear flows. *J. Fluid Mech.*, **51**, 39–61, https://doi.org/10.1017/S0022112072001065.

Holmboe, J., 1962: On the behavior of symmetric waves in stratified shear layers. *Geophys. Publ.*, **24**, 67–113.

Hughes, K. G., J. N. Moum, and E. L. Shroyer, 2020a: Evolution of the velocity structure in the diurnal warm layer. *J. Phys. Oceanogr.*, **50**, 615–631, https://doi.org/10.1175/JPO-D-19-0207.1.

——, ——, and ——, 2020b: Heat transport through diurnal warm layers. *J. Phys. Oceanogr.*, **50**, 2885–2905, https://doi.org/10.1175/JPO-D-20-0079.1.

Kaminski, A. K., and W. D. Smyth, 2019: Stratified shear instability in a field of pre-existing turbulence. *J. Fluid Mech.*, **862**, 639–658, https://doi.org/10.1017/jfm.2018.973.

Kudryavtsev, V. N., and A. V. Soloviev, 1990: Slippery near-surface layer of the ocean arising due to daytime solar heating. *J. Phys. Oceanogr.*, **20**, 617–628, https://doi.org/10.1175/1520-0485(1990)020<0617:SNSLOT>2.0.CO;2.

Lian, Q., W. D. Smyth, and Z. Liu, 2020: Numerical computation of instabilities and internal waves from in situ measurements via the viscous Taylor–Goldstein problem. *J. Atmos. Oceanic Technol.*, **37**, 759–776, https://doi.org/10.1175/JTECH-D-19-0155.1.

Marshall, J., C. Hill, L. Perelman, and A. Adcroft, 1997: Hydrostatic, quasi-hydrostatic, and nonhydrostatic ocean modeling. *J. Geophys. Res.*, **102**, 5733–5752, https://doi.org/10.1029/96JC02776.

Moulin, A. J., J. N. Moum, and E. L. Shroyer, 2018: Evolution of turbulence in the diurnal warm layer. *J. Phys. Oceanogr.*, **48**, 383–396, https://doi.org/10.1175/JPO-D-17-0170.1.

Osborn, T. R., 1980: Estimates of the local rate of vertical diffusion from dissipation measurements. *J. Phys. Oceanogr.*, **10**, 83–89, https://doi.org/10.1175/1520-0485(1980)010<0083:EOTLRO>2.0.CO;2.

Paulson, C. A., and J. J. Simpson, 1977: Irradiance measurements in the upper ocean. *J. Phys. Oceanogr.*, **7**, 952–956, https://doi.org/10.1175/1520-0485(1977)007<0952:IMITUO>2.0.CO;2.

Pham, H. T., and S. Sarkar, 2014: Evolution of an asymmetric turbulent shear layer in a thermocline. *J. Turbul.*, **15**, 449–471, https://doi.org/10.1080/14685248.2014.914216.

Pollard, R. T., P. B. Rhines, and R. O. R. Y. Thompson, 1972: The deepening of the wind-mixed layer. *Geophys. Astrophys. Fluid Dyn.*, **4**, 381–404, https://doi.org/10.1080/03091927208236105.

Price, J. F., R. A. Weller, and R. Pinkel, 1986: Diurnal cycling: Observations and models of the upper ocean response to

diurnal heating, cooling, and wind mixing. *J. Geophys. Res.*, **91**, 8411–8427, https://doi.org/10.1029/JC091iC07p08411.

Salehipour, H., C. P. Caulfield, and W. R. Peltier, 2016: Turbulent mixing due to the Holmboe wave instability at high Reynolds number. *J. Fluid Mech.*, **803**, 591–621, https://doi.org/10.1017/jfm.2016.488.

Sarkar, S., and H. Pham, 2019: Turbulence and thermal structure in the upper ocean: Turbulence-resolving simulations. *Flow Turbul. Combus.*, **103**, 985–1009, https://doi.org/10.1007/s10494-019-00065-5.

Smyth, W. D., and J. Moum, 2002: Shear instability and gravity wave saturation in an asymmetrically stratified jet. *Dyn. Atmos. Oceans*, **35**, 265–294, https://doi.org/10.1016/S0377-0265(02)00013-1.

——, and J. Carpenter, 2019: *Instability in Geophysical Flows*. Cambridge University Press, 338 pp., https://doi.org/10.1017/9781108640084.

——, J. R. Carpenter, and G. A. Lawrence, 2007: Mixing in symmetric Holmboe waves. *J. Phys. Oceanogr.*, **37**, 1566–1583, https://doi.org/10.1175/JPO3037.1.

——, J. N. Moum, and J. D. Nash, 2011: Narrowband oscillations in the upper equatorial ocean. Part II: Properties of shear instabilities. *J. Phys. Oceanogr.*, **41**, 412–428, https://doi.org/10.1175/2010JPO4451.1.

——, J. D. Nash, and J. N. Moum, 2019: Self-organized criticality in geophysical turbulence. *Sci. Rep.*, **9**, 3747, https://doi.org/10.1038/s41598-019-39869-w.

Sobel, A. H., J. Sprintall, E. D. Maloney, Z. K. Martin, S. Wang, S. deSzoeke, B. Trabing, and S. A. Rutledge, 2021: Large-scale state and evolution of the atmosphere and ocean during PISTON 2018. *J. Climate*, **34**, 5017–5035, https://doi.org/10.1175/JCLI-D-20-0517.1.

Soloviev, A., and R. Lukas, 1996: Observation of spatial variability of diurnal thermocline and rain-formed halocline in the western Pacific warm pool. *J. Phys. Oceanogr.*, **26**, 2529–2538, https://doi.org/10.1175/1520-0485(1996)026<2529:OOSVOD>2.0.CO;2.

——, and ——, 1997: Observation of large diurnal warming events in the near-surface layer of the western equatorial Pacific warm pool. *Deep-Sea Res.*, **44**, 1055–1076, https://doi.org/10.1016/S0967-0637(96)00124-0.

Sun, C., W. D. Smyth, and J. N. Moum, 1998: Dynamic instability of stratified shear flow in the upper equatorial Pacific. *J. Geophys. Res.*, **103**, 10 323–10 337, https://doi.org/10.1029/98JC00191.

Sutherland, G., L. Marié, G. Reverdin, K. H. Christensen, G. Broström, and B. Ward, 2016: Enhanced turbulence associated with the diurnal jet in the ocean surface boundary layer. *J. Phys. Oceanogr.*, **46**, 3051–3067, https://doi.org/10.1175/JPO-D-15-0172.1.

Tedford, E. W., J. R. Carpenter, R. Pawlowicz, R. Pieters, and G. A. Lawrence, 2009: Observation and analysis of shear instability in the Fraser River estuary. *J. Geophys. Res. Oceans*, **114**, C11006, https://doi.org/10.1029/2009JC005313..

——, S. MacIntyre, S. D. Miller, and M. J. Czikowsky, 2014: Similarity scaling of turbulence in a temperate lake during fall cooling. *J. Geophys. Res. Oceans*, **119**, 4689–4713, https://doi.org/10.1002/2014JC010135.

Thorpe, S. A., 1978: The near-surface ocean mixing layer in stable heating conditions. *J. Geophys. Res.*, **83**, 2875–2885, https://doi.org/10.1029/JC083iC06p02875.

——, and A. J. Hall, 1977: Mixing in upper layer of a lake during heating cycle. *Nature*, **265**, 719–722, https://doi.org/10.1038/265719a0.

——, and Z. Liu, 2009: Marginal instability? *J. Phys. Oceanogr.*, **39**, 2373–2381, https://doi.org/10.1175/2009JPO4153.1.

Ushijima, Y., and Y. Yoshikawa, 2019: Mixed layer depth and sea surface warming under diurnally cycling surface heat flux in the heating season. *J. Phys. Oceanogr.*, **49**, 1769–1787, https://doi.org/10.1175/JPO-D-18-0230.1.

Van Roekel, L., and Coauthors, 2018: The KPP boundary layer scheme for the ocean: Revisiting its formulation and benchmarking one-dimensional simulations relative to LES. *J. Adv. Model. Earth Syst.*, **10**, 2647–2685, https://doi.org/10.1029/2018MS001336.

Weller, R. A., and J. F. Price, 1988: Langmuir circulation within the oceanic mixed layer. *Deep-Sea Res*, **35A**, 711–747, https://doi.org/10.1016/0198-0149(88)90027-1.

Wijesekera, H. W., D. W. Wang, and E. Jarosz, 2020: Dynamics of the diurnal warm layer: Surface jet, high-frequency internal waves, and mixing. *J. Phys. Oceanogr.*, **50**, 2053–2070, https://doi.org/10.1175/JPO-D-19-0285.1.

Woods, J. D., 1980: Diurnal and seasonal variation of convection in the wind-mixed layer of the ocean. *Quart. J. Roy. Meteor. Soc.*, **106**, 379–394, https://doi.org/10.1002/qj.49710644902.

Yonemitsu, N., G. E. Swaters, N. Rajaratnam, and G. A. Lawrence, 1996: Shear instabilities in arrested salt-wedge flows. *Dyn. Atmos. Oceans*, **24**, 173–182, https://doi.org/10.1016/0377-0265(95)00444-0.